Ion specific tuning of nanoparticle dispersion in an ionic liquid: A structural, thermoelectric and thermo-diffusive investigation.

T. Fiuza,[a,b] M. Sarkar,[a] J.C. Riedl,[a] M. Beaughon,[c] B.E. Torres Bautista,[c]
K. Bhattacharya,[c] F. Cousin,[d] E. Barruet,[e] G. Demouchy,[a,f] J. Depeyrot,[b]
E. Dubois,[a] F. Gélébart,[a] V. Gersteen,[e] G. Mériguet,[a] L. Michot,[a] S. Nakamae,[c]
R. Perzynski,[a,*] and V. Peyre [a]

ELECTRONIC SUPPORTING INFORMATION

S1 Details of sample synthesis

S1.1 NP's characteristics

The synthesised maghemite NPs are prepared by a coprecipitation of iron II and iron III chlorides in water with a strong base according to the process described by Massart[1–3] and in the ESI of Ref[4]. Their size distribution is lognormal and can be determined from magnetisation measurements: median diameter d_0 = 6.9 nm; polydispersity index s = 0.21. The diameter $d_{NP} = \sqrt[3]{\langle d^3 \rangle}$ = 7.4 nm is the third moment of the diameter distribution. The NPs present a number-averaged specific surface $< d^2 > /\rho < d^3 >$ = 154 m^2/g and a NP's saturation magnetisation m_S = 302 kA/m. The principles of preparation of the NPs coated with citric acid in water is the same as in the ESI of Ref[4] and the transfer to EAN keeps all species, removing water by pumping after addition of EAN.

S1.2 Preparation of the concentrated ferrofluids in EAN

These initial dispersions obtained in EAN, at a NP volume fraction close to 1%, are submitted to an ultracentrifugation (UC) at 250 000g (Optima MAX-XP Ultracentrifuge from Beckman Coulter, 25°C), performed during 16, 24 or 32 hours.

For this sample preparation by UC, all samples are weighted at each step in order to allow checking the mass balance. For each UC duration, a clear supernatant is obtained. The remaining dark liquid at the bottom is separated as well as possible by pipetting and homogenised before further use (chemical determinations of the elements and other measurements). For each cation, 3 supernatants and 4 colloidal dispersions (monophasic or not) with average NPs volume fractions between $\sim$ 3.5% and $\sim$ 25% are thus obtained, in addition to the initial ones. These volume fractions are obtained by Inductively Coupled Plasma - Mass Spectroscopy (ICP-MS) determination of iron quantity, the mass balance at the different steps being controlled: (i) before/after drying under vacuum; (ii) before/after UC, (using a density of 5.07 g/cm^3 for maghemite[5]) - See Section S1.3 for more details.

S1.3 Determination of Iron and alkaline ions by ICP-MS

The concentrations of iron and of alkaline ions are determined by Inductively Coupled Plasma - Mass Spectroscopy (ICP-MS) (Thermo Scientific iCAP Q). All dilutions are realised by weight using HNO$_3$ 2 vol%. All solvents and diluting solutions are tested for the absence of ions of interest. The samples are analyzed by external calibration in the range 0.2-25 ppb. The standards are obtained by weight dilution from a multi-element certified concentration solution (Spex, MS2) in HNO$_3$ (2 vol%). For each sample and standard, six runs are performed. The collision cell of the instrument is used to avoid the ArO molecular interference at mass 56. Iron concentration is thus measured on Fe(56) in KED conditions. Lithium, sodium and rubidium are analysed in standard conditions at mass 7 (Li(7)), 23 (Na(23)) and 85 (Rb(85)).

Each dispersion to be analysed is first mixed with HCl 37 vol% in order to dissolve the iron oxide nanoparticles. After 30 minutes

[a] Sorbonne Université, CNRS, Lab. PHENIX, 4 Place Jussieu, F-75005 Paris, France. Email: regine.perzynski@sorbonne-universite.fr

[b] Grupo de Fluidos Complexos, Inst. de Fisíca, Univ. de Brasília, Brasília (DF), Brazil.

[c] Service de Physique de l'Etat Condensé, SPEC, CEA, CNRS, Université Paris-Saclay, CEA Saclay, 91191 Gif sur Yvette, CEDEX, France

[d] Lab. Léon Brillouin - UMR 12 CNRS-CEA CEA-Saclay, 91191 Gif-sur-Yvette, France.

[e] Univ. Paris-Saclay, CEA-CNRS, NIMBE-LIONS, 91191 Gif sur Yvette, France.

[f] Univ. de Cergy Pontoise, Dpt de physique, 33 Bd du Port, 95011 Cergy-Pontoise, France.

sonication in a bath, two dilutions by a factor 5000 are produced, each being then diluted twice by a factor 400. The 4 samples obtained are thus each diluted by a factor $2\,10^6$ and analysed. An average among them is then performed to get the weight concentration of the elements.

The iron and the alkaline ions amounts are determined in the initial samples, and after each ultracentrifugation in the clear supernatants (that contain no nanoparticles) and in the bottom phases that contains concentrated NPs dispersed in the solvent. Everything being weighted, the mass balance of iron and the one of the alkaline ions are then carefully checked. The initial amount is indeed the sum of the amounts in the supernatant and in the bottom phase, after centrifugation. The concentration in all supernatants is identical in all centrifuged samples for a given ion X^+ and independent of the duration of the ultracentrifugation therefore independent on the concentration of the bottom phase. In these bottom phases containing nanoparticles, the concentration of alkaline ions arises from the free and from the adsorbed species. Owing that the concentration of free species is identical to the concentration in the separated supernatant, the difference with the total concentration is found to be proportional to the amount of nanoparticles and is attributed to adsorbed species. The results enable us to conclude that there is an adsorption equilibrium law between the free and the adsorbed alkaline ions.

Note that, whatever the technique used to determine alkaline ions, the determination of sodium remains more difficult than the others due to its ubiquitous presence.

S2 Small Angle Scattering

S2.1 Experimental technique

Small Angle X-ray Scattering (SAXS)

To probe the nanostructure of the colloidal dispersions, SAXS experiments are performed at room temperature at the SWING beamline (SOLEIL Synchrotron, France). An incident beam energy 14666 eV is used with two sample-detector distances, yielding a total range of scattering vector Q extending between 3.2×10^{-3} Å^{-1} and 4×10^{-1} Å^{-1}. For spherical NPs, the scattered intensity can be written as:

$$I(Q,\phi) = (\Delta\rho)^2 \Phi V_{NP} P(Q) S(Q,\Phi) \tag{S1}$$

where $(\Delta\rho)^2$ is the X-ray contrast between NPs and solvent, Φ the NPs' volume fraction, V_{NP} their volume, $P(Q)$ is the NPs' form factor and $S(Q)$ their structure factor. Measurements extrapolated at zero volume fraction enable determining the experimental form factor, that corresponds to $S(Q) = 1$ in Eq. S1. The comparison of $I(Q \rightarrow 0)$ to the value for the form factor indicates whether the overall NP/NP interaction in the sample is repulsive or attractive.

The structure factor extrapolated at $Q = 0$ corresponds to the osmotic compressibility χ of the NP system if the particles are individually dispersed. χ is related to the osmotic pressure Π by:

$$\chi(\Phi) = \frac{kT}{V_{\mathrm{NP}}} \frac{\partial \Phi}{\partial \Pi} \tag{S2}$$

where Π is the osmotic pressure.

Coupled SANS/ DLS measurements at different T's

Static Small Angle Neutron Scattering (SANS) measurements are coupled to Dynamical Light Scattering (DLS) measurements in a furnace, on the PAXY spectrometer at the LLB /Orphée facility (CEA Saclay, France). Both the furnace and a tailored support for a DLS laser remote source (Vascoflex or VascoKin from Cordouan Technologies) are fixed on a rotating table to ensure a reproducible position of the sample, when switching from SANS to DLS. The furnace is filled with nitrogen gas to work under inert atmosphere. The SANS accessible Q-range in this configuration is 0.005 Å^{-1} to 0.2 Å^{-1} in a range of T extending between 25°C and 200°C, the DLS working at $Q = 2.865 \times 10^{-3}$ Å^{-1}. For spherical NPs, the scattered neutron intensity can be written with Eq. S1, $(\Delta\rho)^2$ being now the neutronic contrast between NPs and solvent. The (short / few minutes long) DLS measurements, performed between two SANS measurements at different temperatures, enable checking that the temperature is balanced in the sample before switching to the next SANS spectrum (longer/ 2 hours long). Note that the viscosity drastically decreases with temperature and strongly influences the field DLS correlation function $g_1(t)$, decreasing the relaxation time. As well, any NP's agglomeration would influence it by increasing the relaxation time, on the contrary. * The reproducibility of the correlation function, before and after the SANS measurement, is thus a good marker of the temperature steadiness and of the sample stability.

S2.2 Analysis with Carnahan-Starling model in the case of repulsive interparticle interaction

As explained in the main text, in the case of repulsive interparticle interaction, the compressibility of the dispersions can be described by the Carnahan-Starling development, considering effective hard spheres of diameter d_{eff}. This development of $\chi(\Phi)$ for effective hard

---

* We deduce the field auto-correlation function $g_1(t)$ from the intensity auto-correlation function $G(t)$ using the following expression $g_1(t) \propto \sqrt{G(t) - \mathrm{background}}$.

spheres[6,7] of volume fraction Φ_{eff} is given by:

$$\chi(\Phi) = \chi_{cs}(\Phi_{eff}) = \frac{(1-\Phi_{eff})^4}{1+4\Phi_{eff}+4\Phi_{eff}^2-4\Phi_{eff}^3+\Phi_{eff}^4}. \tag{S3}$$

The second virial coefficient A_2 of the osmotic pressure Π in the dispersion can be obtained from Φ_{eff} without hypotheses on the NPs size :

$$A_2 = A_2^{HS}\frac{\Phi_{eff}}{\Phi}. \tag{S4}$$

where $A_2^{HS} = 4$. The effective volume fraction Φ_{eff} can be also translated in terms of NP diameter d_{NP} and screening length l_S as:

$$\Phi_{eff} = \Phi\frac{d_{eff}^3}{d_{NP}^3} = \Phi\left(1+\frac{2\,l_S}{d_{NP}}\right)^3 \quad \text{with} \quad d_{eff} = d_{NP}+2\,l_S. \tag{S5}$$

S2.3 Dynamic Light Scattering (DLS)

Fig. S1 presents $g_1(t)$ correlation functions measured by DLS (VascoKin, Cordouan Technologies) on the neutron spectrometer, just after the neutron SANS measurement presented in Fig. 2 of the main text at $\Phi = 6.55\%$ with Na^+ counterions. Within the experimental error bar, no evolution is detected at 27°C after the high temperature excursion. The shorter characteristic time of $g_1(t)$ at higher T's is directly related to the decrease of the viscosity of EAN with temperature[8].
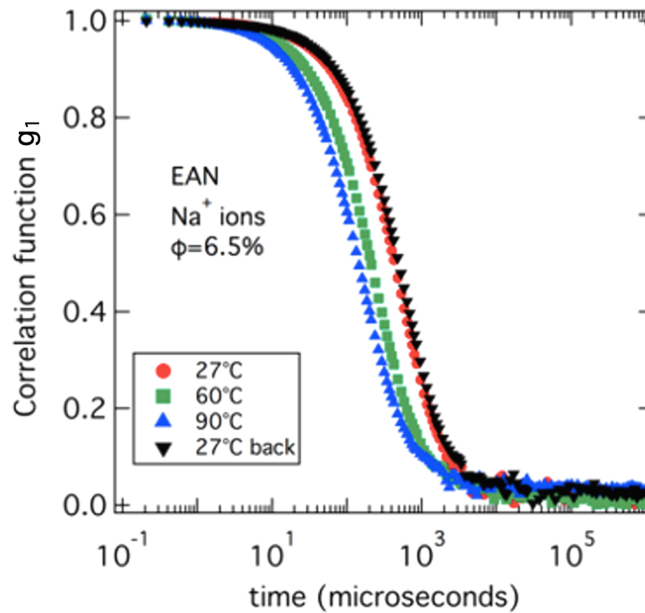

Fig. S1 DLS correlation function g_1 as a function of time t at different temperatures T for a sample in EAN at $\Phi = 6.55\%$ with Na^+ counterions

S2.4 SAXS complementary results

Fig. S2 shows the influence of added water on the SAXS profile of NP's dispersions at $\Phi = 1$ vol% in EAN for the three alkaline ions lithium, sodium and rubidium at room temperature. For 5 vol% of added water, the effect is within the experimental error bar. There is thus a weak influence of added water (within the probed experimental range) on the observed microstructure of the dispersions.

To probe the temperature dependence of the NP-NP attraction in the EAN dispersions with Li^+ counterions, SAXS measurements are performed at the beam line SWING of SOLEIL Synchrotron - France with a sample at $\Phi = 4.3$ %. Fig. S3 confirms the colloidal stability of the sample when the temperature varies from 20 °C up to 80 °C, and back to 20 °C and shows that, within the experimental error bar, there is no evolution of the scattered intensity $I(Q)$, and thus of the NP-NP interaction, in the temperature range.

S3 Forced Rayleigh Scattering

S3.1 Experimental technique

The thermodiffusion measurements are performed using the forced Rayleigh scattering device extensively described in Refs.[9–11], in particular in ESI of Ref.[10], inducing in the liquid sample, periodic spatial modulations of temperature, ΔT, and of NP's volume fraction,
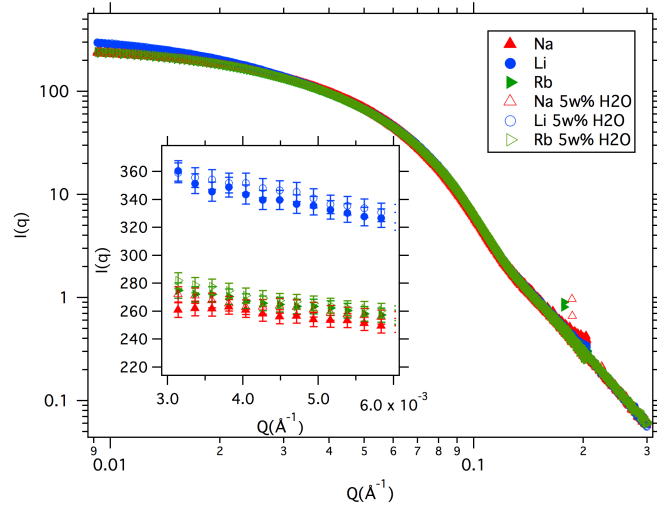
Fig. S2 - Small Angle X-ray Scattering (SAXS) at room temperature for 1vol% dispersions with the three counterions. Dry dispersions and dispersions with 5w% of added water. The inset is the zoom of the low Q region for all samples.
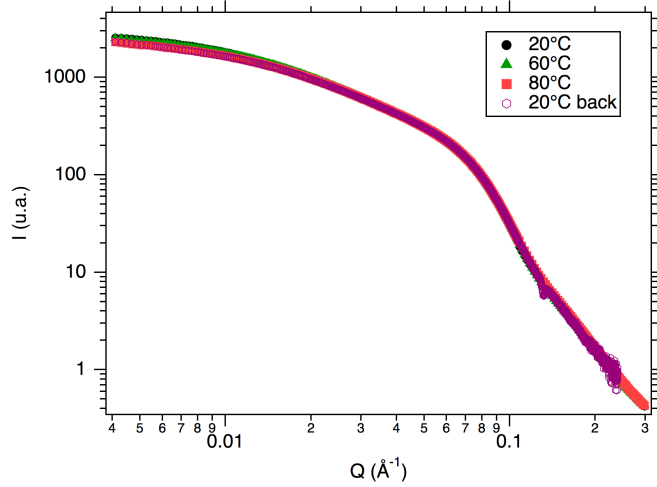

Fig. S3 - Small Angle X-ray Scattering (SAXS) at different temperatures T (given in the legend) for a dispersion with Li^+ counterions at $\Phi = 4.3\%$.

$\Delta\Phi$. The sample is put in an optical cell, thermo-regulated within 22°C-110°C. It can be submitted to a horizontal magnetic field H, homogeneous at the cell-scale and varying from 0 to 100 kA/m. The first order diffraction of a non-absorbing He-Ne laser probes the periodic arrays of temperature and concentration. The thermal grating is created in the dispersion by a high-power lamp (6285-500W -Hg Arc Lamp-Spectra Physics) thanks to the strong optical absorption of maghemite NPs. It is modulated at 8 Hz. The concentration grating is induced in the dispersion by the temperature gradients thanks to the Soret effect according to Eq. S6, the thermal response of the dispersion being faster than the concentration one by orders of magnitude[9,10].

$$\vec{\nabla}\Phi = -\Phi S_T \vec{\nabla}T \tag{S6}$$

The NP's Soret coefficient S_T is determined in the steady state and the mass diffusion coefficient D_m is obtained through the relaxation of the concentration grating after switching off the lamp. The temperature gradients (and thus also the volume fraction ones) are oriented either horizontally or vertically, with the optical cell and gratings being in the vertical plane, to probe the under-field anisotropy of $S_T(H,T)$ and of $D_m(H,T)$. The small values of the modulations $\Delta\Phi \leq 0.06\%$ and $< \Delta T > \leq 0.06$ K, and of the sample thickness ($th = 25\mu$m) prevent the occurrence of any convection or instabilities related to gravity. The spatial period Λ of the gratings ranges between 70 and 145 μm. In-field measurements are performed under the 2D-array conditions at ratios th/Λ, in the range $0.17 \leq th/\Lambda \leq 0.36$ and at magnetic fields H below the 2D magneto-convection threshold[12,13]. S_T measurements are performed in the linear power regime[14] and it is checked that the results are independent of Λ.

S3.2 Diffusion coefficient D_m deduced from FRS relaxation as a function of T in zero applied field

- *Determination of D_m* Diffusion coefficient D_m can be determined by relaxation of FRS on a large range of temperature when the gradient of temperature is abruptly put to zero. In these conditions, the flux $\vec{j}_\Phi$ of NPs under the action the gradient of volume fraction $\vec{\nabla}\Phi$ is:

$$\vec{j}_\Phi = -\frac{1}{\zeta(\Phi,T)}\frac{\partial \Pi V_{NP}}{\partial \Phi}\,\vec{\nabla}\Phi = -D_m(\Phi,T)\,\vec{\nabla}\Phi \tag{S7}$$

where $\zeta(\Phi,T)$ is the friction experienced by the NPs and $D_m(\Phi,T)$ their diffusion coefficient.

In the limit $\Phi \to 0$, there is no interparticle interaction and the Φ's dependencies vanish. Consequently, friction and diffusion coefficient become $\zeta_0(T)$ and $D_{m,0}(T)$. They write respectively:

$$\zeta_0(T) = 3\pi\eta(T)d_H \qquad \text{and} \qquad D_{m,0}(T) = \frac{kT}{\zeta_0(T)}, \tag{S8}$$

η is the viscosity experienced by the nanoparticles. At finite Φ, the diffusion coefficient expresses as:

$$D_m(\Phi,T) = \frac{kT}{\zeta(\Phi,T)\chi(\Phi)} \tag{S9}$$

the compressibility χ given by Eq. S2 being here temperature independent according to conclusions of Section 3.1.2 of main text. The following expression for the friction $\zeta(\Phi,T)$ of hard spheres in hydrodynamic interaction at low volume fractions Φ, typically up to $\sim 5\%$, has been proposed by Batchelor in[15]:

$$\zeta(\Phi,T) = \frac{\zeta_0(T)}{1 - k_F\Phi} \qquad \text{with} \qquad k_F = 6.55, \tag{S10}$$

and an empirical expression to describe the HS friction, valid up to larger volume fractions, has been proposed by Dhont in[16]:

$$\zeta(\Phi,T) = \frac{\zeta_0(T)}{(1-\Phi)^6}. \tag{S11}$$

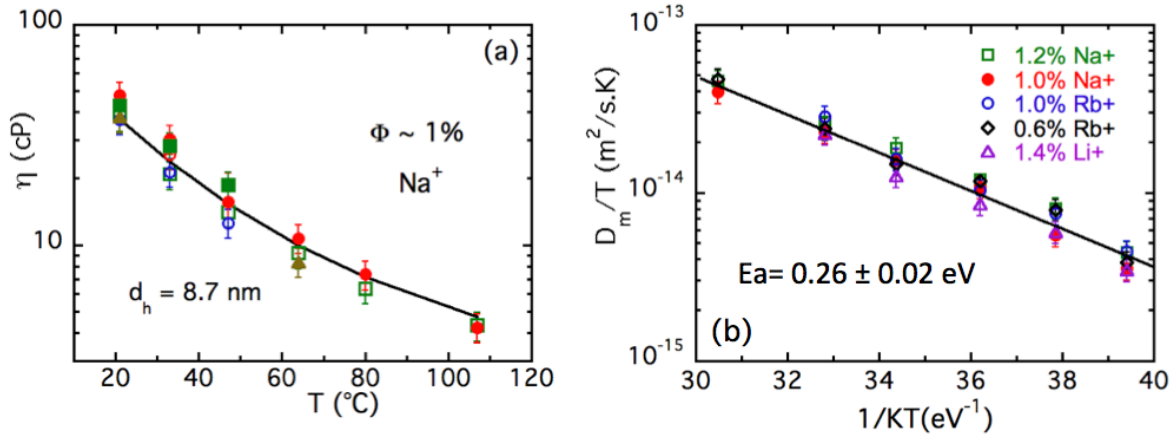- *Results at room T for the various counterions*

Fig. S4 (a) Viscosity $\eta(T)$ experienced by the NPs as deduced from the experiments for various dispersions at $\Phi \sim 1\%$ with Na$^+$ counter-ions (using Eqs. S8, S9 and S10) - full line is bulk EAN viscosity from Ref.[8]; (b) Representation of the reduced diffusion coefficient D_m/T obtained in dispersions at $\Phi \sim 1\%$ as a function of $1/kT$ for the three counterions. The full line corresponds to an exponential Boltzmann fit of the data leading to an mean activation energy $Ea = 0.26 \pm 0.02$ eV/K.

Fig. S4 - (a) shows η, the viscosity experienced by the NPs in the experiment at several Φ's $\sim 1\%$ for Na$^+$ counterions, as a function of T. It is here deduced using Eqs. S8, S9 and S10. In Eq. S10 we use, as hard sphere volume fraction, the value of Φ_{eff} from Section 3.1.1 of main text and $d_H = 8.7$ nm as hydrodynamic diameter. The dispersion viscosity η nicely follows η_{EAN}, the bulk EAN viscosity from Ref.[8].

- *Activation energy of the local viscosity at $\Phi = 1\%$ fitted with the Andrade model*

Fig. S4 - (b) shows the evolution of D_m/T obtained in dispersions at $\Phi \sim 1\%$, as a function of $1/kT$ for the three counterions. D_m/T is at the first order proportional to the inverse of the viscosity of the dispersion if the compressibility χ is supposed T-independent.
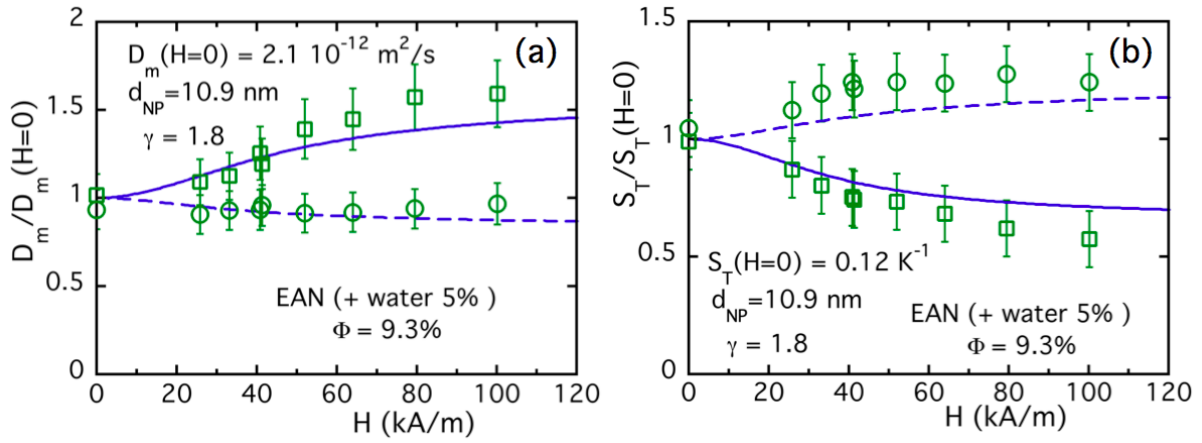
Fig. S5 - Under-field anisotropy of (a) the diffusion coefficient D_m and (b) the Soret coefficient S_T normalised by their values in zero field $(D_m(H = 0) = 2.1 \times 10^{-21} \, m^2 s^{-1}$ and $S_T(H = 0) = 0.12 \, K^{-1})$ at room temperature with a sample at $\Phi = 9.3\%$ with Na^+ counter-ions in EAN with 4% of water. Symbols are experimental data and the lines correspond to the field-adjustments with the formalism of Refs. [11,20,21], the applied field being either parallel (open squares and full lines) or perpendicular (open circle and dashed lines) to the temperature gradients $\vec{\nabla}T$ in the dispersion.

Analysed in the framework of the Andrade model [17], it is adjusted with an Arrhenius law of the form $\propto e^{-Ea/kT}$. The experimental adjustment leads here to $Ea = 0.26 \pm 0.02$ eV/K for the three counterions. This value is slightly larger but rather close to that observed for pure EAN viscosity (21.75 kJ/mol $= 0.22$ eV - see Ref. [18]). It can be also compared to $Ea = 0.20$ eV deduced from the NMR measurements of the diffusion coefficient of translation of EA^+ ions and NO_3^- ions in pure EAN by Filippov et al [19] (see Fig. S12).

S3.3 Under field anisotropy of D_m and S_T

The anisotropy of D_m and that of S_T under field are here probed at room temperature with a sample at $\Phi = 9.3\%$ with Na^+ counterions in a mixture of EAN with a few % of water ($\sim$ 5 wt% - which could slightly reduce the colloidal stability). As shown by Fig. S5, this sample is stable at least up to an applied magnetic fields H of 100 kA/m,. It presents a reversible behaviour when going back to zero field after the high field measurements.

The under-field anisotropy is here described with the model of Ref. [11,20,21]. The parameters used for the adjustment are a dipolar parameter $\gamma = \mu_0 m_s^2 V_{NP}\Phi/kT = 1.8$ together with a magnetic NP diameter of 10.9 nm (larger than its median value as the monodisperse model does not take into account the NP's polydispersity). The corresponding normalised dipolar parameter is $\Psi_{dd} = \gamma/\Phi = 19$, a reasonable value with respect to the sample size-distribution (see some examples in Ref. [22]).

S3.4 Theoretical modelling of $S_T(\Phi, T)$

According to Refs. [21,23–25] and disregarding the negligible term $\frac{1}{\Phi \, kT}\frac{\partial \Pi V_{NP}}{\partial T}$ to a first approximation, S_T can be written:

$$S_T = \chi\left(\frac{\hat{S}_{NP}}{kT} - e\xi_0^{eff}\frac{S_e^{st}}{kT}\right) \tag{S12}$$

where e is the elementary charge and S_e^{st} is the stationary Seebeck coefficient associated to the internal field $\vec{E}^{st} = -S_e^{st}\vec{\nabla}T$ in the conditions of the FRS experiment.

To obtain the stationary Seebeck coefficient in Eq.S12, it is first necessary to write the electro-neutrality of the system, taking into account all dissociated ionic species {i} in the dispersions. These are; EA^+, NO_3^-, X^+ (being here either Na^+, Rb^+ or Li^+) and CH_3COO^- (as we assimilate here the trivalent citrate ion which is rather big to three independent monovalent CH_3COO^- ions, as in Refs [21,24,25]). These species are all monovalent with a charge $z_i = \pm 1$ and a number per unit volume n_i. The NPs are supposed to bear a static effective charge Z_0^{eff}, given by the equation of electroneutrality of the dispersion:

$$Z_0^{eff} \, n_{NP} + \sum_i n_i \, z_i = 0 \tag{S13}$$

where n_{NP} is the number of nanoparticle per unit volume. Z_0^{eff} is of the same sign and the same order of magnitude as the effective dynamic charge ξ_{eff}^0 of Eq.S12.

Using Eq.S13 with the stationary condition of the FRS experiment [23,26], namely a null-flux for each of the present species (NPs and

each kind of free ions), we obtain the stationary Seebeck coefficient as given by:

$$eS_e^{st} = \frac{\sum_i (n_i \, z_i \, \hat{S}_i) + n_{\text{NP}} \, Z_0^{\text{eff}} \, \chi \, \hat{S}_{\text{NP}}}{\sum_i (n_i \, z_i^2) + n_{\text{NP}} \, Z_0^{\text{eff}} \, \chi \, \xi_0^{\text{eff}}} \tag{S14}$$

where $\hat{S}_i$ is the Eastman entropy of transfer of the dissociated species {i} in the dispersion. In the following we disregard the dissociated ions X^+ and CH_3COO^- (initial co- and counter-ions in water) as their contribution is very low in comparison with those of dissociated EA^+ and NO_3^-. Ahead we note as n_+ (resp. n_-) the number per volume unit of positive (resp. negative) dissociated ions. Neglecting at the numerator of Eq.S14, the Eastman entropy of transfer $\hat{S}_+$ and $\hat{S}_-$ of these small ions in front of $\hat{S}_{\text{NP}}$ the Eastman entropy of transfer of the huge NPs (see section S5), we obtain:

$$eS_e^{st} = \frac{i \, n_{\text{NP}} \, |Z_0^{\text{eff}}| \, \chi \, \hat{S}_{\text{NP}}}{2n_i + n_{\text{NP}} \, |Z_0^{\text{eff}}| \, (1 + \chi \, |\xi_0^{\text{eff}}|)}, \tag{S15}$$

here i is the sign of Z_0^{eff}. This expression together with Eq.S12 also leads to :

$$S_{\text{T}} = \chi \frac{\hat{S}_{\text{NP}}}{kT} \left(\frac{2n_i + n_{\text{NP}} \, |Z_0^{\text{eff}}|}{2n_i + n_{\text{NP}} \, |Z_0^{\text{eff}}| \, (1 + \chi \, |\xi_0^{\text{eff}}|)} \right). \tag{S16}$$

This last expression, which is also Eq. 7 of the main text, shows that $\hat{S}_{\text{NP}}$ has the same sign as S_{T}.

S3.5   Soret coefficient as a function of Φ at different T's for the three counterions

In Eq. S16, the compressibility χ is known from the structure study (see Fig. 1-c of the main text) and is independent of T (see Section 3.1.2 of main text), the number of particles is also known and $n_{\text{NP}} = 6\Phi/(\pi d_{\text{NP}}^3)$. The unknown parameters are $\hat{S}_{\text{NP}}$, n_+ and $Z_0^{\text{eff}} = \xi_0^{\text{eff}}$, which are constant parameters independent of Φ. It is intructive to fit the data in the form TS_{T}/χ as a function of Φ. Fig. S6 at room temperature is given as an example. TS_{T}/χ writes as:

$$\frac{TS_{\text{T}}}{\chi} = \frac{\hat{S}_{\text{NP}}}{k} \left(\frac{2n_+ + n_{\text{NP}} \, Z_0^{\text{eff}}}{2n_+ + n_{\text{NP}} \, Z_0^{\text{eff}} \, (1 + \chi \, \xi_0^{\text{eff}})} \right) \tag{S17}$$

Indeed, the shape of the curves (i.e. curvature and position of the minimum) TS_{T}/χ versus Φ is fixed by ξ_0^{eff} and n_+ parameters, while the height of the curve is fixed by $\hat{S}_{\text{NP}}$.

Fig. S7 presents the Soret coefficient S_{T} as a function of volume fraction for the three counterions at various temperatures. As the compressibility χ of the dispersions, S_{T} decreases with Φ whatever T for Na^+ and Rb^+ counterions and increases with Φ whatever T for Li^+, as it is observed in Fig. 5 of the main text at room temperature. The associated values of ξ_0^{eff} and $\hat{S}_{\text{NP}}$ are presented and discussed in section 4.2.2 of main text.

The stationary Seebeck coefficient S_e^{st} deduced from the fitting of Fig. S7 is presented in Fig. S8 for Na^+ and Rb^+ counterions at the different temperatures. In the experimental range of Φ and T, S_e^{st} is found to vary between 2.5 and 3 mV/K without a clear dependence in temperature. We recall here that this bulk thermal contribution is induced by the internal electric field and cannot be measured in a thermoelectric experiment. In the thermocell, the metallic electrodes creates surface effects, such as the electronic double-layer formation, which mask the bulk internal electric field.
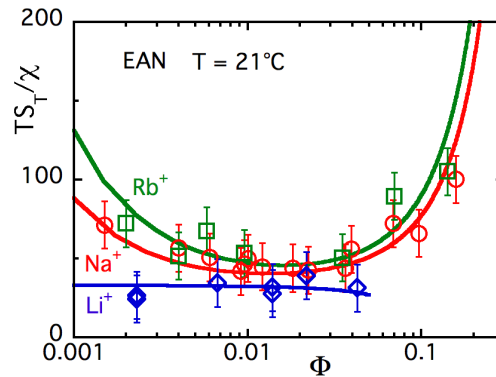

Fig. S6 Φ-dependence of TS_{T}/χ at room temperature for the three counterions - Full lines are the adjustments obtained with the formalism of Section 3.2.4 of main text and the parameters of Table 2 of main text.
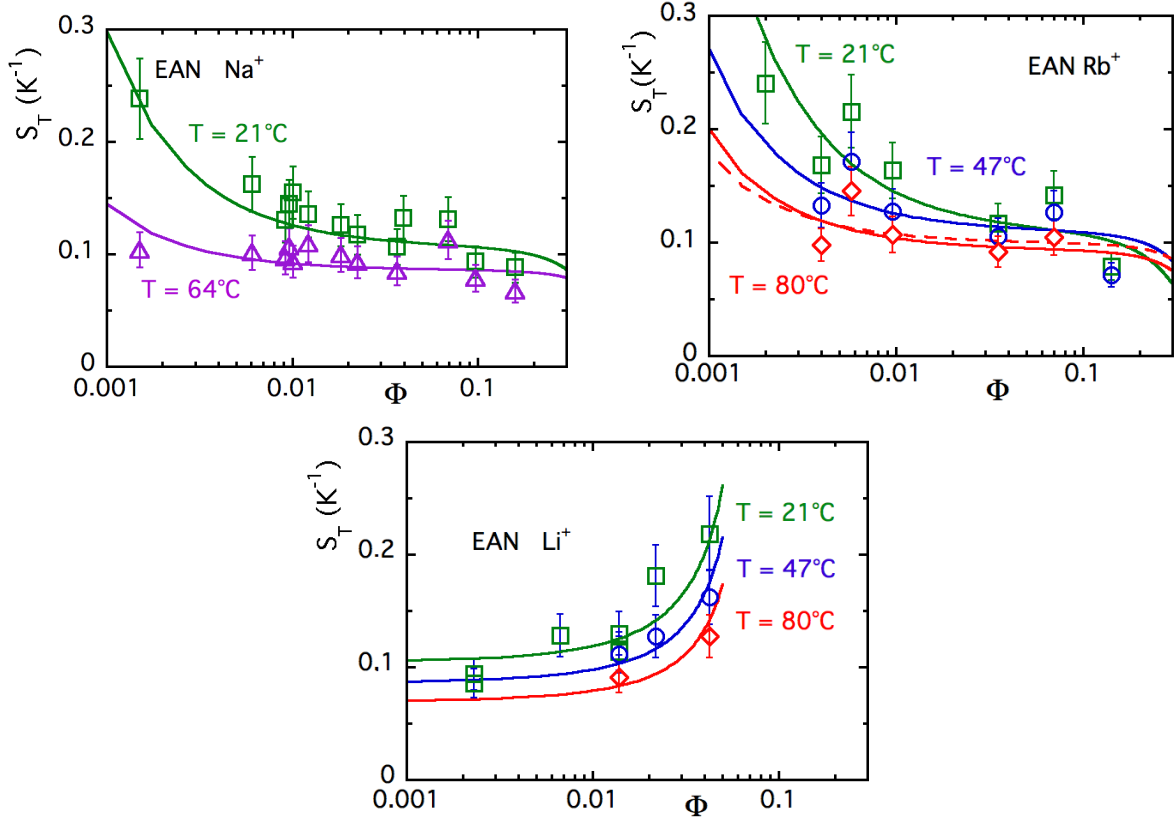
Fig. S7 Evolution of the Soret coefficient S_T as a function of volume fraction for the three counterions at various temperatures; Full and dashed lines are adjustments with the present formalism.
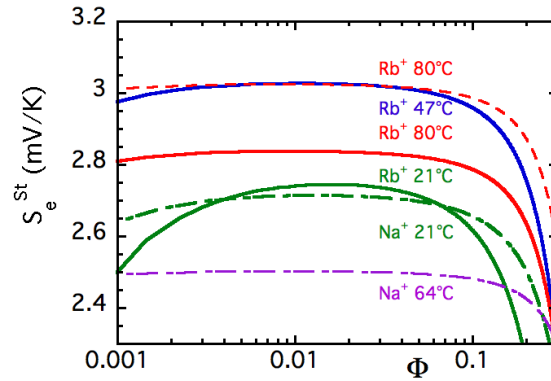

Fig. S8 - Stationary Seebeck coefficient S_e^{st} as a function of the volume fraction as deduced from the adjustments for Na$^+$ and Rb$^+$ counterions at the different temperatures of Fig. S7.

S3.6 Soret coefficient in the low and high effective NP charge limits

Let us note that Eq.S17 can be simplified as follows, in the low and high effective NP charge limits.

- When the effective charge ξ_0^{eff} is small with a low volume fraction Φ (thus with $n_{NP} \rightarrow 0$), then $2n_+ \gg n_{NP} Z_0^{eff}$ and Eq.S17 becomes:

$$S_T = \chi \frac{\hat{S}_{NP}}{kT}. \tag{S18}$$

This condition is fulfilled here only for the attractive sample with lithium. S_T and χ vary in the same way with Φ, increasing here in the case of lithium counterions (see Fig. 5 of main text).

- When the effective charge is larger and if the volume fraction is high enough, $2n_+ \ll n_{NP} Z_0^{eff}$, Eq.S17 becomes:

$$S_{\mathrm{T}} \sim \frac{\hat{S}_{\mathrm{NP}}}{kT} \frac{1}{\frac{1}{\chi} + \xi_0^{\mathrm{eff}}} \sim \frac{\hat{S}_{\mathrm{NP}}}{kT} \frac{1}{\xi_0^{\mathrm{eff}}} \quad \text{provided} \ \chi \xi_0^{\mathrm{eff}} \gg 1. \tag{S19}$$

These conditions are fulfilled for the dispersion with Na^+ and Rb^+ around $\Phi = 10\%$. In this limit, the compressibility no longer matters. From Equation S19, it results that $\hat{S}_{\mathrm{NP}}/\xi_0^{\mathrm{eff}}$ is around 0.1 kT K^{-1}, whatever T in the experimental range, which is fairly compatible with the conclusions obtained from the thermoelectric measurements of Section 3.2 of the main text.

S4 Thermoelectric measurements

S4.1 Experimental technique

The thermo-electrochemical (TE) device used here is fully described in Refs.[25,27]. A thermocell of circular section 0.28 cm^2 is filled with the NP dispersion in EAN together with the redox couple salt LiI/I$_2$ at 10 mM [†]. The two ends of the thermocell are sealed with conducting electrodes for exchanging electrons with the redox couple to generate electricity. The two electrodes are maintained at two different temperatures T_{cold} and T_{warm}, ranging between 20°C and 50°C, to induce a temperature gradient in the cell with a temperature difference $\Delta T = T_{\mathrm{warm}} - T_{\mathrm{cold}}$. In open-circuit, the voltage difference ΔV induced across the thermocell under a temperature difference ΔT is related to the Seebeck coefficient Se by:

$$Se = -\Delta V / \Delta T \tag{S20}$$

Connecting the electrodes to a discharge resistor, power out-put measurements can also be realised. They are performed by recording the evolution of ΔV while changing the value of the resistor put in parallel to the thermocell, the electric current I in the thermocell being obtained with Ohm law.

In a thermocell containing charged colloidal particles, two terms predominantly contribute to the Seebeck coefficient Se, namely the thermogalvanic contribution $Se_{\mathrm{TG}} = -\Delta S_{rc}/e$ and the thermoelectro-diffusion Se_{TED}. The thermo-galvanic contribution ΔS_{rc} originates from the T-dependent reaction entropy of the (reversible) redox couple at the electrode surface, which can be expressed by the Nernst equation (see[28,29]). With time, the thermoelectro-diffusion contribution Se_{TED} evolves from an initial state (before any gradient of concentration is created in the thermocell) towards a steady state (corresponding to the Soret equilibrium of all the species in the thermocell), respectively corresponding to $Se_{\mathrm{TED}}^{\mathrm{ini}}$ and $Se_{\mathrm{TED}}^{\mathrm{st}}$. Here, we only consider the initial Se due to the fact that 1) Se_{TED} is screened from the electrode due to the rearrangement of charged ions in the Soret equilibrium state[20] and 2) the long time scale to establish the Soret equilibrium in our experimental conditions (3-5 days)[29]. $Se_{\mathrm{TED}}^{\mathrm{ini}}$ writes as:

$$Se_{\mathrm{TED}}^{\mathrm{ini}} = \Sigma_i \frac{t_i \hat{S}_i}{e \xi_i} \tag{S21}$$

where t_i, ξ_i and $\hat{S}_i$ denote the Hittorf transport number, the effective dynamic charge, and the Eastman entropy of transfer of the ith charged species (particles, ions, molecules, etc.) in the dispersion, respectively. Separating the term $\Delta Se_{\mathrm{TED}}^{\mathrm{ini}}(\Phi)$ associated to the NPs from the other contributions of the free ions and molecules $Se_{\mathrm{TED}}^{\mathrm{ini}}(\Phi = 0)$, we obtain for the NP's contribution to $Se_{\mathrm{TED}}^{\mathrm{ini}}$:

$$\Delta Se_{\mathrm{TED}}^{\mathrm{ini}}(\Phi) = Se_{\mathrm{TED}}^{\mathrm{ini}}(\Phi) - Se_{\mathrm{TED}}^{\mathrm{ini}}(\Phi = 0) = t_{\mathrm{NP}}(\Phi) \frac{\hat{S}_{\mathrm{NP}}}{e \xi_0^{\mathrm{eff}}} \tag{S22}$$

S4.2 Thermoelectric measurements - complementary results

Fig. S9 presents experimental determinations of $Se_{\mathrm{TED}}^{\mathrm{ini}}$ as a function of the NP's volume fraction Φ for Na^+ and Li^+ counterions, which are performed at a mean temperature 25°C with electrodes at $T_{\mathrm{cold}} = 20°C$ and $T_{\mathrm{warm}} = 30°C$ (heating from the top). They show that the NP contribution $\Delta Se_{\mathrm{TED}}^{\mathrm{ini}}$ is positive and that the ratio $\hat{S}_{\mathrm{NP}}/kT \xi_0^{\mathrm{eff}}$ range between 0.05 K^{-1} and 0.15 K^{-1}, with a mean value of the order of 0.1 K^{-1}.

When a discharge resistor is put in parallel to the thermo-cell, the output voltage decreases while the electric current intensity increases. The evolution of the voltage V obtained for various resistor values is presented in Fig. S10-a as a function of current intensity I, for dispersions with Na^+ counterions at different NP's volume fractions Φ and for a temperature difference $\Delta T = 30°C$ between the two electrodes with a mean temperature $T_{\mathrm{mean}} = 30°C$. The corresponding power output P per unit surface of the electrode is presented in Fig. S10-b as a function I. This figure illustrates the fact that introducing the NPs reduces the power.

For dispersions with Li^+ counterions, measurements are performed at $\Phi = 0.3\%$. Fig. S11-a (resp. Fig. S11-b) shows in that case the evolution of $V(I)$ (resp. the evolution of the power density P as a function of the current density), for different T_{cold} /T_{warm} couples. The larger ΔT, the larger the maximum output. If a power density P of the same order of magnitude is obtained with Na^+ and with Li^+ counterions in similar conditions of Φ, T_{cold} and T_{warm}, a closer comparison (see Fig. 4 of the main text) shows that at $\Phi = 0.3\%$, P is 50% larger with Li^+ than with Na^+, illustrating the influence of the NP/IL interface on the TE behaviour.

[†] Tests with NaI/I$_2$ have been performed in[25] showing comparable results, however less stable from an electrochemical point of view.
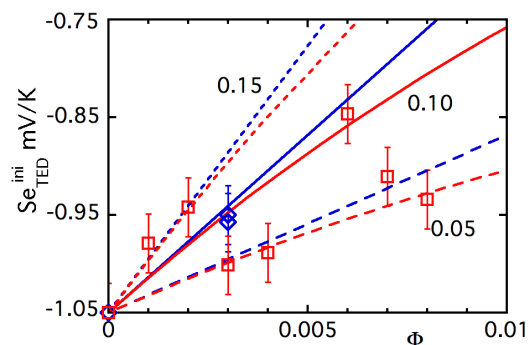
Fig. S9 Se_{TED}^{ini} as a function of NP volume fraction Φ for Na$^+$ (red squares and red lines) and Li$^+$ (blue diamonds and blue lines) counterions. Symbols: Experimental results obtained at a mean temperature 25°C with electrodes at $T_{cold} = 20$°C and $T_{warm} = 30$°C (heated from the top); Lines are adjustments with Eq. S22 (see main text for details) using several values (in K^{-1}) of the ratio $\hat{S}_{NP}/kT\xi_0^{eff}$, given in black in the figure.
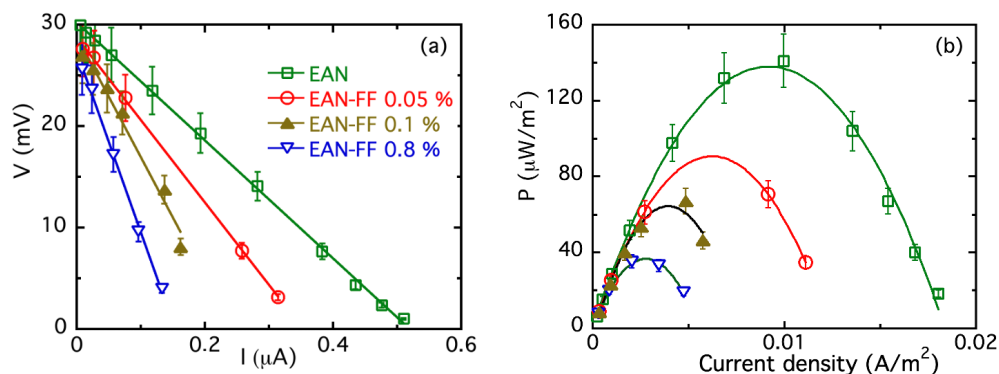

Fig. S10 Dispersion in EAN at various Φ's with Na$^+$ counterions - voltage as a function of current intensity (a) and power per surface unit (as a function of current density (b), measured with $T_{cold} = 20$°C and $T_{warm} = 50$°C - heated from the top.
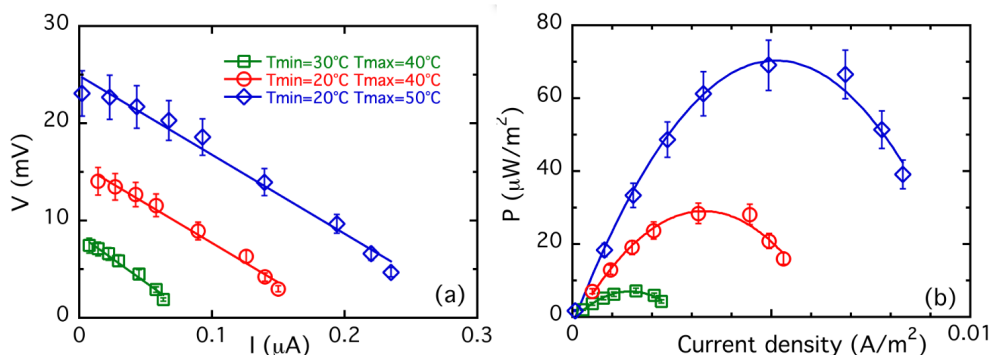

Fig. S11 - Dispersion in EAN at $\Phi = 0.3\%$ with Li$^+$ counterions - voltage V as a function current intensity I (a) and power per unit surface P as a function of current density (b), for different T_{cold} / T_{warm} couples (see legend) - heated from the top.

S5   Eastman entropy of transfer of EA$^+$ and NO$_3^-$ in pure EAN

According to Würger in Ref.[30], who describes thermodiffusion in pure ionic liquids as driven by thermally activated formation of short-lived vacancies[31] with hopping dynamics between neighbour sites (thermally activated jumps to neighbour sites) with an enthalpy barrier (= the activation energy) directly related to the heat of transport of the cations and anions of the IL. Thus the activation energy $Ea = 0.20 - 0.22$ eV of EAN[18,19] (see Fig. S12) is both the enthalpy barrier and the heat of transport Q^* of the ions EA$^+$ and NO$_3^-$,
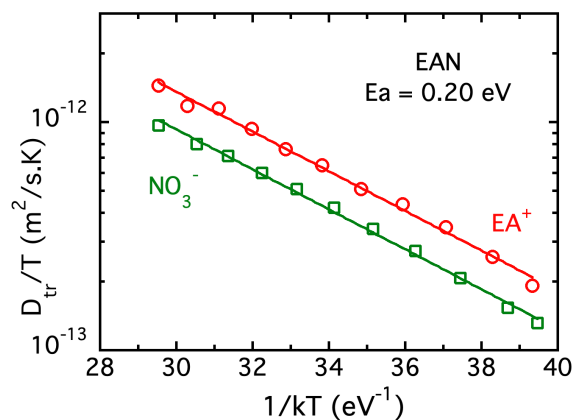
Fig. S12 - Log-lin representation of the diffusion coefficient of translation D_{tr} over T of EA^+ ions and NO_3^- ions as a function of $1/kT$; Symbols: NMR data from the ESI of Filippov et al[19]; Full lines: Best exponential adjustments of the data leading to a slope $Ea = 0.20$ eV for both ions.

$\hat{S}_{EAN} = \hat{S}_{EA^+} - \hat{S}_{NO_3^-} = Q^*/T$ [‡]. At room temperature we obtain $\hat{S}_{EAN}/kT \sim 0.03$ K^{-1}. This value can be compared to the tabulated values of NO_3^- ($\hat{S}_{NO_3^-}/kT = -0.002$ K^{-1} in water at room temperature) and to the experimental evaluation for EA^+ (in water at room temperature from FRS measurements) $\hat{S}_{EA^+}/kT \sim +0.012$ K^{-1} (unpublished result from PHENIX lab). At room temperature, we obtain here an Eastman entropy of transfer for EA^+ and NO_3^- ion which is slightly larger than in water; However, it is still much smaller than the NP's Eastman entropy of transfer in Table 2 of the main text, strengthening the hypothesis of Section S3.4 where the Eastman entropy of transfer of the small ions were neglected in front of $\hat{S}_{NP}$.

S6   Specific features of additive ions in ILs

If additional species X^+ are present in the IL, here, Li^+, Na^+ or Rb^+ (at a molar ratio X^+/EA^+ around 1%), they can modify the bulk and/or interface with a solid, as shown by some recent studies. When added in bulk EAN, salts such as lithium nitrate[32,33], zinc chloride[34] or cerium nitrate[35] are found in polar domains and surrounded by nitrate anions. Among alkaline ions, mainly lithium was studied and it was shown that lithium is a structure breaker for EAN[32]. In propylammonium nitrate IL (PAN), for example, such metallic cations are known to replace PA^+ at the mica-IL interface regardless of the charge and size of the cation[36]. This is due to their stronger electrostatic interaction with mica than PA^+, which also seems to favour their desolvation when adsorbed on the surface. In another study,[37] AFM force measurements on a mica surface evidence changes in the thickness of the layers, their organisation and the friction inside the first layers when 1w% of $LiNO_3$ was added to EAN. This amount of lithium is of the same order as that used in our experiments and modifies the interfacial structure. Li^+ also modifies the organisation of the first layer in EMIM TFSI (1-ethyl-3-
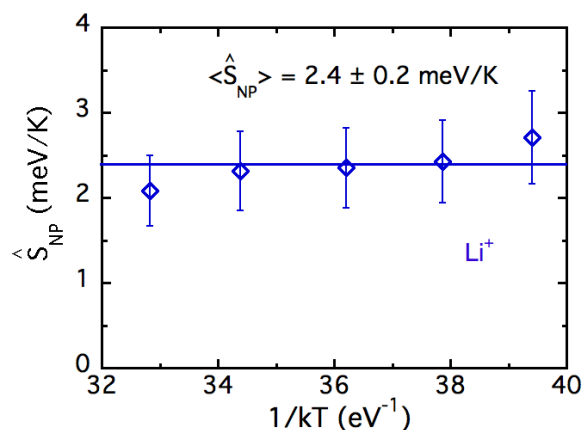

Fig. S13 - NP's Eastman entropy of transfer $\hat{S}_{NP}$ as a function of $1/kT$ for Li^+ counterions as deduced from the adjustments of $S_T(\Phi, T)$ of Section S3.5; Full line corresponds to the average value of $\hat{S}_{NP}$

.

[‡] Providing that as many EA^+ and NO_3^- ions contribute to thermally driven charge transport[26,30]

methylimidazolium bistriflimide) on graphene, replacing the $EMIM^+$ ions[38]. Its behaviour on the mica surface can however strongly differ when changing the IL. In EMIM TFSI, Li^+ is solvated by $TFSI^-$ and does not interact with mica[39]. On the contrary, in EMIM FSI (1-ethyl-3-methylimidazolium bis(fluorosulfonyl)imide), Li^+ prefers the mica surface. The behaviour of these added species thus results from a delicate balance between the different forces between species and is quite difficult to predict.

S7 NP's Eastman entropy of transfer with Li^+ as counterions

Fig. S13 present the temperature dependence of the NP's Eastman entropy of transfer $\hat{S}_{NP}$ in the case of Li^+ counterions deduced from Eq. S18 within the low NP charge approximation. The second term in bracket in Eq. S12 is thus neglected and the compressibility χ is taken independent of T (as shown experimentally at the first order in Section S2.4). The variations of $\hat{S}_{NP}$ are presented as a function of $1/kT$. Contrarily to what is found for Na^+ and Rb^+ in the main text, no significant dependence of $\hat{S}_{NP}$ on T is observed with these Li^+ counterions.

Notes and references

1 R. Massart, *I.E.E.E., Trans. on Magn.*, 1981, **2**, 1247–1248.

2 R. Massart, *C. R. Acad. Sci. Paris*, 1980, **291**, 1–3.

3 R. Massart, E. Dubois, V. Cabuil and E. Hasmonay, *J. Magn. Magn. Mat.*, 1995, **149**, 1–5.

4 C. L. Filomeno, M. Kouyaté, V. Peyre, G. Demouchy, A. Campos, R. Perzynski, F. A. Tourinho and E. Dubois, *J. Phys. Chem. C*, 2017, **121**, 5539–5550.

5 U. Schwertmann and R. Cornell, *Iron oxides in the laboratory*, John Wiley and Sons Inc, Hoboken - New Jersey - USA, 2008.

6 N. Carnahan and K. Starling, *J. Chem. Phys.*, 1970, **53**, 600.

7 J. A. Barker and D. Henderson, *J. Chem. Phys.*, 1967, **47**, 4714–4721.

8 J. Smith, G. Webber, G. Warr and R. Atkin, *J. Phys. Chem. B*, 2013, **117**, 13930–13935.

9 G. Demouchy, A. Mezulis, A. Bée, D. Talbot, J. Bacri and A. Bourdon, *J. Phys. D: Appl. Phys.*, 2004, **37**, 1417–1428.

10 M. Sarkar, J. C. Riedl, G. Demouchy, F. Gélébart, G. Mériguet, V. Peyre, E. Dubois and R. Perzynski, *Eur. Phys. J. E*, 2019, **42**, 979–2989.

11 T. Fiuza, M. Sarkar, J. C. Riedl, A. Cēbers, F. Cousin, G. Demouchy, J. Depeyrot, E. Dubois, F. Gélébart, G. Mériguet, R. Perzynski and V. Peyre, *Soft Matter*, 2021, **17**, 4566–4577.

12 D. Zablotsky, *PhD thesis*, Faculty of Physics and Mathematics - Univ. of Latvia, Riga - Latvia, 2012.

13 D. Zablotsky, A. Mezulis and E. Blums, *C. R. Mecanique*, 2013, **341**, 449–454.

14 W. Luo, T. Du and J. Huang, *Phys. Rev. Lett.*, 1999, **82**, 4134–4137.

15 G. K. Batchelor, *J. Fluid Mech.*, 1982, **119**, 379–408.

16 J. K. G. Dhont, *An Introduction to Dynamics of Colloids*, Elsevier Science, 1996, pp. 1–642.

17 E. da C. Andrade, *Nature*, 1930, **125**, 309–310.

18 R. Zarrougui, M. Dhahbi and D. Lemordant, *J. Solution Chem.*, 2015, **44**, 686–702.

19 A. Filippov, O. Gnezdilov, N. Hjalmarsson, O. Antzutkin, S. Glavatskih, I. Furo and M. Rutland, *Phys. Chem. Chem. Phys.*, 2017, **19**, 25853–25858.

20 T. Salez, S. Nakamae, R. Perzynski, G. Mériguet, A. Cēbers and M. Roger, *Entropy*, 2018, **20**, 405.

21 M. Kouyaté, C. Filomeno, G. Demouchy, G. Mériguet, S. Nakamae, V. Peyre, M. Roger, A. Cēbers, J. Depeyrot, E. Dubois and R. Perzynski, *Phys. Chem. Chem. Phys.*, 2019, **21**, 1895–1903.

22 G. Mériguet, F. Cousin, E. Dubois, F. Boué, A. Cēbers, B. Farago and R. Perzynski, *J. Phys. Chem. B*, 2006, **110**, 4378–4386.

23 B. Huang, M. Roger, M. Bonetti, T. J. Salez, C. Wiertel-Gasquet, E. Dubois, R. C. Gomes, G. Demouchy, G. Mériguet, V. Peyre, M. Kouyaté, C. L. Filomeno, J. Depeyrot, F. A. Tourinho, R. Perzynski and S. Nakamae, *J. Chem. Phys.*, 2015, **143**, 054902.

24 R. Cabreira-Gomes, A. da Silva, M. Kouyaté, G. Demouchy, G. Mériguet, R. Aquino, E. Dubois, S. Nakamae, M. Roger, J. Depeyrot and R. Perzynski, *Phys. Chem. Chem. Phys.*, 2018, **20**, 16402–16413.

25 K. Bhattacharya, M. Sarkar, T. J. Salez, S. Nakamae, G. Demouchy, F. Cousin, E. Dubois, L. Michot, R. Perzynski and V. Peyre, *ChemEngineering*, 2020, **4**, 5 1–25.

26 A. Majee and A. Würger, *Phys. Rev. E*, 2011, **83**, 061403.

27 T. J. Salez, B. T. Huang, M. Rietjens, M. Bonetti, C. Wiertel-Gasquet, M. Roger, C. L. Filomeno, E. Dubois, R. Perzynski and S. Nakamae, *Phys. Chem. Chem. Phys.*, 2017, **19**, 9409–9416.

28 W. Nernst, *Z. Phys. Chem.*, 1889, **4**, 129–181.

29 T. Salez, M. Kouyaté, C. L. Filomeno, M. Bonetti, M. Roger, G. Demouchy, E. Dubois, R. Perzynski, A. Cēbers and S. Nakamae, *Nanoscale Adv.*, 2019, **1**, 2979–2989.

30 A. Würger, *Phys. Rev. Lett.*, 2021, **126**, 068001 1–5.

31 A. Abbot, *Chem. Phys. Chem.*, 2004, **5**, 1242.

32 R. Hayes, S. A. Bernard, S. Imberti, G. G. Warr and R. Atkin, *J. Phys. Chem. C*, 2014, **118**, 21215–21225.

33 T. Méndez-Morales, J. Carrete, O. Cabeza, O. Russina, A. Triolo, L. Gallego and L. Varela, *J. Phys. Chem. B*, 2014, **118**, 761–770.

34 P. D'Angelo, A. Zitolo, F. Ceccacci, R. Caminiti and G. Aquilanti, *J. Chem. Phys.*, 2011, **135**, 154509.

35 A. Serva, V. Migliorati, R. Spezia and P. D'Angelo, *Chem. Eur. J.*, 2017, **23**, 8424–8433.

36 S. McDonald, A. Elbourne, G. Warr and R. Atkin, *Nanoscale*, 2016, **8**, 906–914.

37 N. Hjalmarsson, R. Atkin and M. W. Rutland, *The Journal of Physical Chemistry C*, 2016, **120**, 26960–26967.

38 A. Elbourne, S. McDonald, K. Voïchovsky, F. Endres, G. G. Warr and R. Atkin, *ACS Nano*, 2015, **9**, 7608–7620.

39 A. M. Smith and S. Perkin, *The Journal of Physical Chemistry Letters*, 2015, **6**, 4857–4861.